Qubit interference at avoided crossings: The role of driving shape and bath coupling

Ralf Blattmann,[1] Peter Hänggi,[1] and Sigmund Kohler[2]
[1]*Institut für Physik, Universität Augsburg, Universitätsstraße 1, D-86153 Augsburg, Germany*
[2]*Instituto de Ciencia Materiales de Madrid, CSIC, Cantoblanco, E-28049 Madrid, Spain*
(Received 18 September 2014; published 9 April 2015)

We derive the structure of Landau-Zener-Stückelberg-Majorana (LZSM) interference patterns for a qubit that experiences quantum dissipation and is additionally subjected to time-periodic but otherwise general driving. A spin-boson Hamiltonian serves as the model, which we treat with a Bloch-Redfield master equation in the Floquet basis. It predicts resonance peaks whose form depends significantly on the operator through which the qubit couples to the bath. The Fourier transforms of the LZSM patterns exhibit arc structures which reflect the shape of the driving. These features are captured by an effective time-independent Bloch equation which provides an analytical solution. Moreover, we determine the decay of these arcs as a function of dissipation strength and temperature.

DOI: 10.1103/PhysRevA.91.042109 PACS number(s): 03.65.Yz, 03.67.−a, 85.25.Cp, 73.21.La

I. INTRODUCTION

The spectrum of a bistable quantum system as a function of the detuning typically forms avoided crossings. In particular in the regime between adiabatic following and nonadiabatic transitions, sweeping the detuning can induce a complex tunneling dynamics. Its archetype is a two-level system with a sweep linear in time for which the probability for nonadiabatic transitions is given by the famous Landau-Zener formula [1–4]. It predicts a splitting of the wave function into a superposition of the adiabatic qubit states, which means that the avoided crossing acts like a beam splitter. Replacing the linear switching by an ac field results in a series of avoided crossings, so that the wave function splits and recombines repeatedly—the quantum mechanical analog of a Mach-Zehnder interferometer [5]. The resulting LZSM interference has been demonstrated in various experiments with solid-state qubits [6–13].

Going beyond the mere demonstration of interference, Landau-Zener-Stückelberg-Majorana (LZSM) interferometry can be employed as a tool to determine the dephasing time of a charge qubit. The analysis of the interference pattern may be performed in "real space," i.e., as a function of detuning and amplitude [12], or in Fourier space [14]. The latter type of analysis is based on the observation that the Fourier transforms of LZSM patterns exhibit arc structures with a characteristic decay [15]. By comparing measured and computed patterns for a qubit, one can determine the inhomogeneous broadening as well as the faster decoherence induced by substrate phonons [14]. Since this procedure takes considerable numerical effort, any analytic knowledge may be helpful.

In this work, we reveal how the qubit-bath coupling operator and the shape of the driving influence the LZSM interference pattern. In Sec. II we describe the qubit with a time-dependent spin-boson model [16] and introduce the Floquet-Bloch-Redfield formalism that provides our numerical solutions. Section III is devoted to the LZSM pattern in real space which is governed by the coupling operator to the bath. In Sec. IV we demonstrate that its Fourier transform, by contrast, mainly reflects the shape of the driving. Finally, in Sec. V, we determine the decay of the arcs as a function of the bath parameters.

II. MODEL AND MASTER EQUATION

A. Qubit in a time-dependent field

We consider a qubit under the influence of a periodic driving described by the Hamiltonian

$$H(t) = \hbar \begin{pmatrix} \epsilon_0 & \Delta/2 \\ \Delta/2 & Af(t) \end{pmatrix}, \tag{1}$$

where Δ is the tunnel coupling between the two levels which experience a modulated detuning $\epsilon_0 - Af(t)$ with shape $f(t) = f(t+T)$, driving period $T = 2\pi/\Omega$, amplitude A, and static detuning ϵ_0. Without loss of generality, we assume that $f(t)$ vanishes on average. The gauge chosen in Eq. (1) is convenient for qualitative discussions, while the equivalent symmetrized Hamiltonian $\tilde{H}(t) = \frac{\hbar}{2}\{\epsilon_0 - Af(t)\}\sigma_z + \frac{\hbar\Delta}{2}\sigma_x$ is preferable for the numerical treatment.

While the most prominent example is the monochromatic $f(t) = \cos(\Omega t)$, our aim is to investigate LZSM interference for general periodic driving. In our numerical examples, we consider besides the purely harmonic driving with $f_0(t) = \cos(\Omega t)$ also the shapes

$$f_1(t) = \cos(\Omega t) + 0.1\cos(3\Omega t), \tag{2a}$$

$$f_2(t) = \cos(\Omega t) + \cos(2\Omega t), \tag{2b}$$

$$f_3(t) = \sin(\Omega t) + \sin(2\Omega t), \tag{2c}$$

where f_1 and f_2 are symmetric functions, i.e., they obey $f(t_0 + t) = f(t_0 - t)$ for $t_0 = 0$ and for $t_0 = T/2$. By contrast, $f_3(t_0 + t) = -f_3(t_0 - t)$ is antisymmetric. While f_1 modifies the pure cosine driving only slightly, the other two shapes are qualitatively different because they possess several maxima and minima per driving period. As we discuss below in Sec. IV, this has consequences for the structures observed in Fourier space; see Figs. 1(g)–1(i).

B. System-bath model

The influence of the environment on the system is modeled by a bath of harmonic oscillators given by the Hamiltonian $H_{\rm env} = H_b + H_{\rm int}$ with $H_b = \sum_\nu \hbar\omega_\nu a_\nu^\dagger a_\nu$, and

$$H_{\rm int} = \frac{1}{2} X \sum_\nu \hbar\lambda_\nu (a_\nu^\dagger + a_\nu), \tag{3}$$

 ©2015 American Physical Society

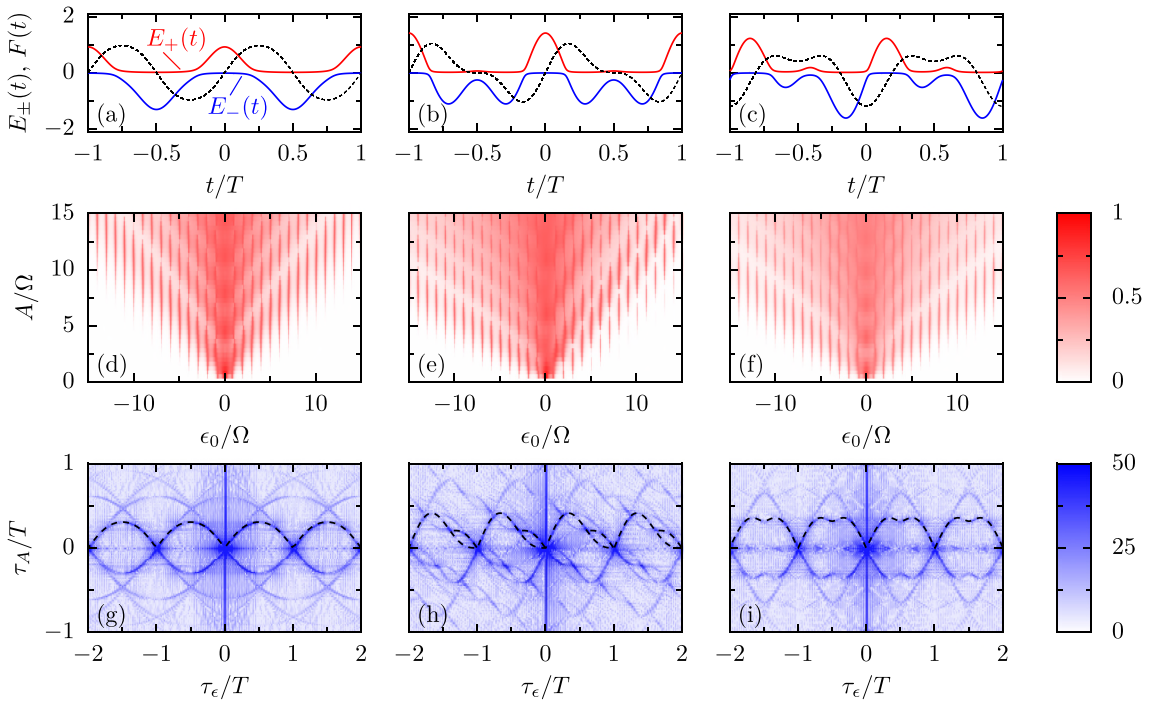

FIG. 1. (Color online) (a)–(c) Adiabatic energies $E_\pm(t)$ (red and blue solid lines) of the Hamiltonian (1) in units of $\hbar\Omega$ for vanishing static detuning, $\epsilon_0 = 0$, and the driving shapes $f_1(t)$–$f_3(t)$ in Eq. (2). The dashed black line marks the integral of the driving $F(t)$ in units of $1/\Omega$. (d)–(f) Resulting nonequilibrium populations in ϵ_0-A space. (g)–(i) Two-dimensional (2D) Fourier transform $W(\tau_\epsilon,\tau_A)$ of the interference patterns, defined in Eq. (23). The dashed lines in the upper half plane mark the analytic expressions for the arc structure derived in Sec. IV. The patterns are computed with the stationary solution of the Bloch-Redfield master equation for the tunnel matrix element $\Delta = 0.5\Omega$, dissipation strength $\alpha = 10^{-3}$, temperature $1/\beta = 0.1\hbar\Omega$, and transverse qubit-bath coupling, i.e., $X = \sigma_x$ in Eq. (3).

where ω_ν are the frequencies of the oscillators, while $\hbar\lambda_\nu$ are the system-oscillator coupling energies. For the qubit operator X that couples to the bath, we mainly consider σ_x and σ_z as well as a linear combination of the two. According to their orientation on the Bloch sphere with respect to the driving, we refer to the coupling as transverse (σ_x) and longitudinal (σ_z), respectively. Moreover we assume that system and environment are initially uncorrelated, i.e., we choose an initial condition of the Feynman-Vernon type, $\rho_{\rm tot}(t_0) = \rho(t_0) \otimes R_{\rm env,eq}$ for the total system density operator $\rho_{\rm tot}$, with $\rho(t_0)$ being the initial reduced density operator of the qubit, while $R_{\rm env,eq} \propto \exp(-\beta H_b)$ is the Gibbs state of the bath with inverse temperature β.

Starting from the Liouville–von Neumann equation $i\hbar\dot\rho_{\rm tot} = [H(t) + H_{\rm env}, \rho_{\rm tot}]$ for the total density matrix and applying standard techniques, one can derive the Markovian weak-coupling master equation [17]

$$\begin{aligned}\frac{d}{dt}\rho &= \mathcal{L}(t)\rho \\ &= -\frac{i}{\hbar}[H(t),\rho] - \frac{1}{4}\int_0^\infty d\tau(\mathcal{S}(\tau)[X,[\tilde X(t-\tau,t),\rho]] \\ &\quad + \mathcal{A}(\tau)[X,\{\tilde X(t-\tau,t),\rho\}]),\end{aligned} \tag{4}$$

where $\{A,B\} = AB + BA$ denotes the anticommutator and $\tilde X(t',t)$ is a shorthand notation for $U^\dagger(t,t')XU(t,t')$, with U being the propagator for the coherent qubit dynamics. The influence of the environment is subsumed in the symmetric and the antisymmetric bath correlation functions,

$$\begin{aligned}\mathcal{S}(\tau) &= \frac{1}{2}\langle\{B(\tau),B(0)\}\rangle_{\rm eq} \\ &= \frac{1}{\pi}\int_0^\infty d\omega J(\omega)\coth(\hbar\omega\beta/2)\cos(\omega\tau),\end{aligned} \tag{5}$$

$$\begin{aligned}\mathcal{A}(\tau) &= \frac{1}{2}\langle[B(\tau),B(0)]\rangle_{\rm eq} \\ &= \frac{1}{\pi}\int_0^\infty d\omega J(\omega)\sin(\omega\tau),\end{aligned} \tag{6}$$

respectively, with the collective bath coordinate $B(t) = \sum_\nu \lambda_\nu\{a_\nu^\dagger \exp(i\omega_\nu t) + a_\nu \exp(-i\omega_\nu t)\}$. The angular brackets $\langle\cdots\rangle_{\rm eq}$ denote the average with respect to the thermal equilibrium of the environment. In a continuum limit we consider the Ohmic spectral density $J(\omega) = \pi\sum_\nu \lambda_\nu^2\delta(\omega-\omega_\nu) \equiv 2\pi\alpha\omega e^{-\omega_c/\omega}$ with the dimensionless dissipation strength α, while the high-frequency cutoff ω_c eventually is taken to infinity.

C. Bloch-Redfield theory in the Floquet basis

Since the system Hamiltonian is periodic in time we can apply the Floquet theorem, which states that the corresponding Schrödinger equation possesses a fundamental set of solutions of the form $|\Psi_\alpha(t)\rangle = e^{-i\varepsilon_\alpha t/\hbar}|\Phi_\alpha(t)\rangle$, with the quasienergies ε_α and the Floquet states $|\Phi_\alpha(t)\rangle = |\Phi_\alpha(t+T)\rangle$ [16].

They can be calculated from the eigenvalue equation $\{H(t) - i\hbar\partial_t\}|\Phi_\alpha(t)\rangle = \varepsilon_\alpha|\Phi_\alpha(t)\rangle$. Expressing the master equation (4) in the Floquet basis $\{|\Phi_\alpha(t)\rangle\}$ [16,17] yields

$$\frac{d}{dt}\rho_{\alpha\beta}(t) = \sum_{\alpha'\beta',k} e^{-ik\Omega t}\mathcal{L}^{(k)}_{\alpha\beta,\alpha'\beta'}\rho_{\alpha'\beta'}(t) \tag{7}$$

with the density matrix element $\rho_{\alpha\beta} = \langle\Phi_\alpha(t)|\rho|\Phi_\beta(t)\rangle$ and

$$\begin{aligned}\mathcal{L}^{(k)}_{\alpha\beta,\alpha'\beta'} &= -i(\varepsilon_{\alpha'} - \varepsilon_{\beta'})\delta_{\alpha,\alpha'}\delta_{\beta,\beta'}\delta_{0,k} \\ &+ \sum_{k'}(N_{\alpha\alpha',k'} + N_{\beta\beta',k'-k})X_{\alpha\alpha',k'}X_{\beta'\beta,k-k'} \\ &+ \delta_{\beta,\beta'}\sum_{k',\beta''} N_{\beta''\alpha',k-k'}X_{\alpha\beta'',k'}X_{\beta''\alpha',k-k'} \\ &+ \delta_{\alpha,\alpha'}\sum_{k',\alpha'} N_{\alpha''\beta',k'-k}X_{\beta'\alpha'',k-k'}X_{\alpha''\beta,k'},\end{aligned} \tag{8}$$

the kth Fourier coefficient of the Liouville operator. We have introduced the transition matrix elements

$$X_{\alpha\beta,k} = \frac{1}{T}\int_0^T dt\, e^{ik\Omega t}\langle\Phi_\alpha(t)|X|\Phi_\beta(t)\rangle \tag{9}$$

and $N_{\alpha\beta,k} = N(\varepsilon_\alpha - \varepsilon_\beta + k\hbar\Omega)$ with $N(\omega) = \alpha\omega n_{\rm th}(\omega)$ as well as the bosonic thermal occupation number $n_{\rm th}(\omega) = (e^{\beta\hbar\omega} - 1)^{-1}$.

In the long-time limit, the system relaxes to a steady state which obeys the time periodicity of the driving, $\rho_\infty(t) = \rho_\infty(t+T)$. Hence we can use the Fourier decomposition $\rho_\infty(t) = \sum_k e^{-ik\Omega t}\rho^{(k)}$ of the density operator to obtain the set of linear equations

$$-i\hbar k\Omega\rho^{(k)}_{\alpha\beta} = \sum_{\alpha',\beta',k'}\mathcal{L}^{(k-k')}_{\alpha\beta,\alpha'\beta'}\rho^{(k')}_{\alpha'\beta'}. \tag{10}$$

This master equation avoids the common moderate [17] or full [18] rotating-wave approximation with respect to the driving frequency Ω and, hence, is rather reliable [19]. In our case, numerical convergence is already obtained with $|k| \leqslant 5$, i.e., for truncation at the fifth sideband, even when the Floquet states may contain many more relevant sidebands. Thus the numerical effort for solving Eq. (10) stays at a tolerable level.

D. Excitation probability

For the visualization of the LZSM interference pattern, one may in the absence of dissipation consider time-averaged transition probabilities from a particular initial state [5]. In the presence of a heat bath, however, the system state is in the long-time limit typically independent of the initial state. Therefore, we consider time averages of observables such as populations, e.g., of the diabatic state $|\uparrow\rangle$, or the excited state of the undriven qubit, $|e\rangle$. Since in the vast part of the parameter space considered, the qubit is strongly biased, i.e., $\Delta \ll |\epsilon_0|$, the choice is of minor practical relevance. We here consider the latter, namely, the time-averaged probability for the qubit being in the excited state as a function of the static detuning ϵ_0 and the driving amplitude A,

$$P_{\rm ex}(\epsilon_0, A) = \frac{1}{T}\int_0^T dt\,\langle e|\rho_\infty(t)|e\rangle, \tag{11}$$

where $\rho_\infty(t)$ is the T-periodic long-time solution of the master equation. Thus, $P_{\rm ex}$ directly relates to the Fourier coefficients in the Floquet basis, $\rho^{(k)}_{\alpha\beta}$, which we obtain by solving Eq. (10).

III. INTERFERENCE PATTERN IN ENERGY SPACE

In order to give a first impression of our results, we depict in Figs. 1(d)–1(f) the LZSM interference patterns for the driving shapes in Eq. (2) and a transverse qubit-bath coupling. All three patterns exhibit resonance peaks whenever the detuning ϵ_0 matches with a multiple of the driving frequency. As a further condition for a significant nonequilibrium population, the amplitude must be so large that it reaches the avoided level crossing, which is the case for $\min[f(t)] < \epsilon_0/A < \max[f(t)]$. The peaks depend strongly on the amplitude and for certain values of A/Ω they may even vanish. This represents a generalization of the coherent destruction of tunneling found for sinusoidal driving [20], a phenomenon responsible for the characteristic vertical structure of LZSM patterns [5] which, in turn, can be explained within a Landau-Zener scenario [21]. Comparing Figs. 1(d)–1(f), we can conclude that the patterns look very similar, despite the rather different driving shapes which are visible in the adiabatic energies of the qubit Hamiltonian (1) depicted in Figs. 1(a)–1(c). The main differences stem from the fact that the harmonics with frequency 2Ω may shift the maximum and the minimum value of $f(t)$ and, thus, affect the condition for significant excitations discussed above. For the driving shape f_2, this condition depends on the sign of ϵ_0, which explains the asymmetry of the pattern in Fig. 1(e), which was also observed in Ref. [22].

A. Influence of the qubit-bath coupling

In Fig. 2, we compare patterns for transverse and longitudinal qubit-bath coupling, i.e., the coupling via σ_x and σ_z, respectively. Since we already noticed that the patterns in energy space are not very sensitive to the shape of the driving, we here restrict ourselves to the purely harmonic $f_0(t) = \cos(\Omega t)$. Let us first consider the transverse coupling. The resulting pattern [Fig. 2(a)] is characterized by resonance islands which as a function of the detuning ϵ_0 are Lorentzians. As a function of the amplitude A, their shape follows approximately the squares of Bessel functions. This behavior was predicted for the current through ac-gated double quantum dots [14,23] and for the nonequilibrium population of a driven two-level system [5]. Moreover, it has been observed in various experiments [6,8,9,11,14,15].

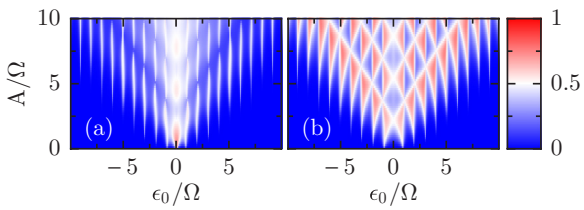

FIG. 2. (Color online) Nonequilibrium population $P_{\rm ex}$ as a function of the detuning ϵ_0 and the driving amplitude A for $f(t) = \cos(\Omega t)$. The qubit-bath coupling $H_{\rm int}$ is determined by $X = \sigma_x$ (a) and $X = \sigma_z$ (b), while $\Delta = 0.5\Omega$, $\alpha = 10^{-3}$, and $1/\beta = 0.1\hbar\Omega$.

If the bath couples longitudinally with respect to the driving, i.e., when both the ac field and the environment enter via σ_z, the pattern changes qualitatively. As it can be appreciated in Fig. 2(b), the Lorentzian peaks turn into a triangular structure. This kind of bath coupling should be relevant for a charge qubit in a Cooper pair box driven by an ac gate voltage while being sensitive to environmental charge fluctuations. LZSM patterns for this setup have been measured in Refs. [7,24] and exhibit similarities with Fig. 2(b). Recent experiments [25] have obtained such triangular patterns with much higher resolution.

As a generalization of these two system-bath couplings, we also considered a bath coupling via the operator

$$X = \sigma_x \cos\theta + \sigma_z \sin\theta. \tag{12}$$

The mixing angle θ varies from 0 to $\pi/2$, where the limits $\theta = 0$ and $\theta = \pi/2$ correspond to the transverse and the longitudinal cases. This model captures, e.g., a superconducting charge qubit that interacts capacitively as well as inductively with the environmental circuitry. Then it is intriguing to know which dissipative influence dominates the LZSM interference. For this purpose, we define the normalized overlap between the pattern for σ_x coupling and the pattern for the coupling operator in Eq. (12) as

$$r_x(\theta) = \frac{\left(P_{\rm ex}^x \middle| P_{\rm ex}^X\right)}{\sqrt{\left(P_{\rm ex}^x \middle| P_{\rm ex}^x\right)\left(P_{\rm ex}^X \middle| P_{\rm ex}^X\right)}}, \tag{13}$$

where $(P|Q) = \int d\epsilon\, dA\, P(\epsilon,A)Q(\epsilon,A)$ denotes the inner product between two functions in ϵ-A space. To compare the mixed case with the pure σ_z coupling we define $r_z(\theta)$ accordingly. Obviously, these quantities possess the limits $r_x(0) = 1 = r_z(\pi/2)$. LZSM patterns generally have in common that their main contribution stems from regions in which a resonance condition is fulfilled. Thus, the overlap of apparently different patterns generally is quite appreciable (typically up to 0.9 for pattern such as those in Fig. 2). Significantly larger values, however, are found only when the shape of the individual peaks is also similar.

The result shown in Fig. 3 reveals that upon increasing θ from $\theta = 0$, i.e., augmenting the influence of σ_z, the pattern remains close to that of Fig. 2(a). By contrast, the pattern for σ_z coupling is more sensitive to a small admixture of σ_x. Thus, unless the bath coupling via σ_z is much larger, we find the "usual" interference pattern of Fig. 2(a). This is consistent with the fact that, in most experiments, one indeed finds such a LZSM pattern with Lorentzians [6,8,9,15]. Notice, however, that this reasoning does not necessarily apply to LZSM patterns for the average current through open double quantum dots [11,14], because there the dominating incoherent dynamics is the electron tunneling between the quantum dots and the leads. Moreover, the Hilbert space for a transport setup is larger since it must comprise states with different electron number.

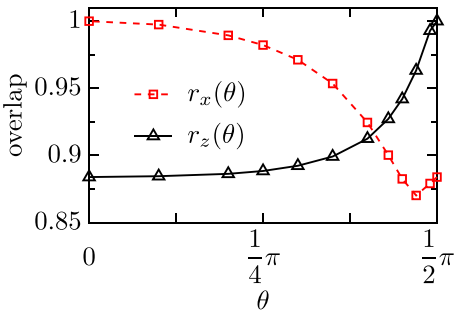

FIG. 3. (Color online) Overlap of the interference pattern for the mixed coupling (12) with the patterns for the coupling operators σ_x (squares) and σ_z (triangles) as a function of the mixing angle. All other parameters are as in Fig. 2.

Let us emphasize that the observed significant dependence of the long-time solution on the coupling is found even in the limit of very weak qubit-bath coupling and, hence, it is beyond a mere higher-order effect in the dissipation strength α. This is in clear contrast to the stationary solution of the Bloch-Redfield equation for a time-independent problem, which generally is the grand canonical state, while possible deviations are of the order α [26]. Nevertheless, we will be able to derive an effective time-independent Bloch equation for the driven qubit which captures the influence of the bath coupling operator even quantitatively.

B. Analysis of the resonance peaks

While the two-dimensional interference patterns in Figs. 1(d)–1(f) and 2 provide a comprehensive picture, the details of the resonance peaks are better visible in the horizontal slices shown in Fig. 4. They reveal that the peaks for transverse coupling indeed are Lorentzians, while for longitudinal coupling, the peaks are antisymmetric. Moreover,

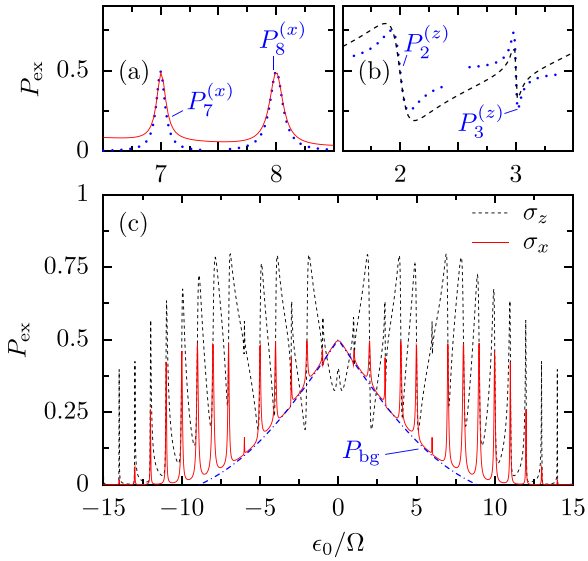

FIG. 4. (Color online) Nonequilibrium population $P_{\rm ex}$ shown in Fig. 2 as a function of the detuning ϵ_0 for the driving amplitude $A = 10\Omega$. (a) Comparison between numerical result with σ_x coupling obtained with the Bloch-Redfield master equation (solid red) and the analytical solution (20) for the resonances with $n = 7,8$ (dotted blue). (b) Comparison between numerical result with σ_z coupling (dashed black) and the analytical solution (22) for $n = 2,3$ (dotted blue). (c) Numerical results for σ_x and σ_z coupling plotted together with the analytical result for the off-resonant background predicted by Eq. (15).

we witness a triangular-shaped background with a roughly linear decay in $|\epsilon_0|$ while being practically independent of the tunneling Δ. Our aim is to explain these features within the Bloch equations for the qubit derived in the Appendix. We restrict the discussion to the limit of very low temperatures for which the interference patterns are most pronounced.

1. *Off-resonant background*

We start our considerations by noticing that, at low temperatures, the dissipative dynamics is mainly a decay towards the qubit ground state. Since for small tunneling Δ and large amplitude A, the (adiabatic) qubit levels form avoided crossings, the states $|\downarrow\rangle$ and $|\uparrow\rangle$ take turns in having lower energy; cf. the upper row of Fig. 1. Within an adiabatic description, we employ the Bloch equation (A4) and replace the ϵ-dependent rates by their instantaneous values to obtain for the z component of the Bloch vector $\vec{s} = \mathrm{tr}(\vec{\sigma}\rho)$ the equation of motion

$$\dot{s}_z = -\Gamma[\epsilon(t)]s_z - \pi\alpha\epsilon(t), \tag{14}$$

where $\epsilon(t) = \epsilon_0 - Af(t)$. If the decay is sufficiently slow, we can replace the time-dependent coefficients by their time averages $\overline{\epsilon(t)} = \epsilon_0$ and $\bar{\Gamma} \equiv \overline{\Gamma[\epsilon(t)]} \approx \alpha(2A + \epsilon_0^2/A)$, where the latter results from a Taylor expansion in ϵ_0/A. Then the steady-state solution $s_z(\infty) = \pi\alpha\epsilon_0/\bar{\Gamma}$ corresponds to the nonequilibrium population

$$P_{\mathrm{bg}} = \frac{1}{2} - \frac{\pi|\epsilon_0|A}{4A^2 + 2\epsilon_0^2}. \tag{15}$$

The dash-dotted line in Fig. 4(c) shows that this estimate indeed describes the triangular-shaped background rather well which, in turn, confirms the underlying adiabatic picture.

The adiabatic approximation underlying the derivation of Eq. (15) implies that this result holds in between the resonances. Close to the resonances, we have to follow a different path. This implies that we finally obtain a piecewise-defined analytical solution which, nevertheless, provides a global picture.

2. *Lorentzian peaks for the transverse coupling via σ_x*

An analytical expression for the resonance peaks can be found within an approximation scheme for close-to-resonant excitation [5,23]. For a bath coupling via σ_x, the calculation is essentially the one given in the Appendix of Ref. [5]. We sketch it briefly so that we can later highlight the differences between σ_x coupling and σ_z coupling.

Embarking with the master equation (4) we consider the limit $|\epsilon_0| \gg \Delta$ and assume that the driving frequency is close to resonance, i.e., $n\Omega = (\epsilon_0^2 + \Delta^2)^{1/2} \approx \epsilon_0$. In this regime the tunneling contribution, proportional to Δ, represents a perturbation to the free dynamics governed by $\frac{1}{2}\{\epsilon_0 - Af(t)\}\sigma_z$. In order to capture the coherent dynamics in large part, we apply the unitary transformation $U(t) = \exp\{-i\phi(t)\sigma_z/2\}$ with the time-dependent phase $\phi(t) = n\Omega t + AF(t)$, where

$$F(t) = \int_0^t dt'\, f(t') \tag{16}$$

obeys the T periodicity of the driving because $f(t)$ by definition vanishes on average. Then we obtain the interaction picture Hamiltonian $U^\dagger(t)H(t)U(t) - i\hbar U^\dagger(t)\dot{U}(t)$. Averaging over the driving period T results in the effective Hamiltonian

$$H_{\mathrm{eff}} = -\frac{\hbar\delta_n}{2}\sigma_z + \frac{\hbar\Delta_n}{2}\sigma_x, \tag{17}$$

with the detuning $\delta_n = n\Omega - \epsilon_0$ and the effective tunnel matrix element

$$\Delta_n(A) = \frac{\Delta}{T}\int_0^T dt\, e^{in\Omega t - iAF(t)}. \tag{18}$$

The latter obviously is the nth Fourier coefficient of $\Delta\exp\{-iAF(t)\}$, a property that will prove useful. This generalizes the result for purely harmonic driving, $\Delta_n = \Delta J_n(A/\Omega)$ with J_n the nth-order Bessel function of the first kind, to arbitrary but periodic shapes $f(t)$. The corresponding equation of motion for the Bloch vector reads $\dot{\vec{s}} = \vec{B}_{\mathrm{eff}} \times \vec{s}$, where $\vec{B}_{\mathrm{eff}} = (\Delta_n, 0, -\delta_n)^T$.

For the dissipative dynamics, we distinguish two limiting cases. First, during the stage at which the qubit passes through the crossing, the tunneling term $\frac{\Delta}{2}\sigma_x$ dominates in the Hamiltonian (1), while the qubit-bath coupling essentially commutes with the Hamiltonian. Thus, it induces pure dephasing but no decay. Since for an Ohmic bath the dephasing rate (A7) is proportional to the temperature, it can be neglected in the low-temperature limit under consideration.

For most of the time, however, the qubit Hamiltonian is dominated by the term proportional to σ_z so that the bath causes transitions between the eigenstates of σ_z. We describe them by the Bloch equation (A4) which together with the effective coherent dynamics reads

$$\dot{\vec{s}} = \begin{pmatrix} -\Gamma/2 & -\delta_n & 0 \\ \delta_n & -\Gamma/2 & \Delta_n \\ 0 & -\Delta_n & -\Gamma \end{pmatrix}\vec{s} - \begin{pmatrix} 0 \\ 0 \\ \Gamma \end{pmatrix}. \tag{19}$$

Notice that since we are interested only in the stationary state, we can ignore a possible driving-induced renormalization of the decay rates [27] and treat Γ as a phenomenological parameter. However, we wish to stress that our numerical treatment captures this renormalization. The steady state $\vec{s}(\infty)$ is easily obtained by matrix inversion and provides the nonequilibrium population, reading

$$P_n^{(x)} = \frac{1}{2}\frac{\Delta_n^2/2}{(\epsilon_0 - n\Omega)^2 + \Delta_n^2/2 + \Gamma^2/4}. \tag{20}$$

While this expression holds close to the nth resonance, it vanishes far away. Therefore, focusing on the peaks and ignoring P_{bg}, the global picture is simply given by the sum of the contributions of all resonances and reads $P_{\mathrm{ex}}^{(x)} = \sum_n P_n^{(x)}$. Expressions like the one in Eq. (20) have been found not only for nonequilibrium populations of driven qubits [5,8,13,15] but also for the dc current through double quantum dots [12,14,23].

In Fig. 4(a), we compare the numerically computed interference pattern for σ_x coupling with the analytical solution (20) at various resonances. While close to the resonances, i.e., for $\delta_n \ll \Delta$, the agreement is almost perfect, we observe small deviations between the resonances which mainly stem from the off-resonant background discussed above. Notice that our

analytical solutions (15) and (20) cannot be simply added, because they hold in different regimes.

3. *Antisymmetric resonances for the longitudinal coupling via σ_z*

For longitudinal coupling, the situation is complementary to the transverse case. Outside the crossing, the bath couples to a good quantum number of the qubit and, thus, creates pure dephasing negligible at low temperatures. Therefore, dissipative transitions are induced only close to the crossing where the qubit Hamiltonian (1) is dominated by σ_x. Consequently, as compared to the case discussed above, the relevant part of the qubit Hamiltonian and the bath coupling operator are interchanged. Accordingly, the x and the z components of the dissipative terms in Eq. (19) are interchanged as well (a formal derivation along the lines of the Appendix is straightforward). This yields the Bloch equation

$$\dot{\vec{s}} = \begin{pmatrix} -\Gamma & -\delta_n & 0 \\ \delta_n & -\Gamma/2 & \Delta_n \\ 0 & -\Delta_n & -\Gamma/2 \end{pmatrix} \vec{s} - \begin{pmatrix} \Gamma \\ 0 \\ 0 \end{pmatrix}, \tag{21}$$

whose stationary solution corresponds to the nonequilibrium population

$$P_n^{(z)} = \frac{1}{2} + \frac{(\epsilon_0 - n\Omega)\Delta_n}{(\epsilon_0 - n\Omega)^2 + 2\Delta_n^2 + \Gamma^2/2}. \tag{22}$$

Since now the qubit decay occurs only during the short stages when the levels cross, the phenomenological rate Γ is expected to be considerably smaller than for σ_x coupling.

In Fig. 4(b), we compare the numerically computed interference pattern obtained with σ_z coupling with the analytical solution (22) for $n = 2,3$. Again, close to a resonance the analytics and the numerical solution agree rather well. Far from resonance, however, expression (22) decays only slowly and the global picture is beyond the simple summation of all $P_n^{(z)}$. Exactly on resonance, i.e., for $\epsilon_0 = n\Omega$, the second term of Eq. (22) vanishes and, hence, the excitation probability becomes $P_{\rm ex}^{(z)} = 1/2$ for all n. This fact together with the asymmetry of the structure implies that close to each resonance, we find a region with $P_{\rm ex}^{(z)} > 1/2$. Such population inversion has been found also for driven qubits with other structureless bath spectral densities [28] and may be induced by the bath [29].

4. *Qubit-bath coupling via σ_y*

For completeness we also consider a bath coupling via the Pauli matrix σ_y. It induces dissipative transitions between both the eigenstates of σ_x and those of σ_z. Therefore, the corresponding Bloch equation is a combination of Eqs. (19) and (21). A simplification comes from the focus on parameter regimes in which the avoided crossings are well separated, i.e., in which the tunnel coupling Δ is small such that for most of the time the qubit Hamiltonian is dominated by the contribution proportional to σ_z. Under this condition, the Bloch equation for σ_y coupling will be mainly of the form (19) with the nonequilibrium population essentially given by Eq. (20), i.e., we expect to find $P_n^{(y)} \approx P_n^{(x)}$.

In order to confirm this conjecture, we have computed the stationary state for σ_y coupling and the parameters used in Fig. 2. The result is practically indistinguishable from Figs. 2(a) and 4(a) (not shown). This is reflected by a normalized overlap between these patterns close to unity. To be specific, we find the value $r \simeq 0.996$.

IV. INTERFERENCE PATTERN IN FOURIER SPACE

In the previous section, we found that the interference patterns in real space depend only weakly on the shape of the driving, while the qubit-bath coupling has a strong influence. The 2D Fourier transform of these patterns [Figs. 1(g)–1(i)] provides a complementary picture in which the shape of the driving dominates. For the symmetric driving functions f_1 and f_2, we find a pronounced arc structure at $\tau_A = 2F(\tau_\epsilon/2)$ and $\tau_A = 2F(\tau_\epsilon/2 + T/2)$; cf. the black dashed lines in Figs. 1(a) and 1(b). They can be explained within the stationary-phase treatment of the LZSM interference scenario [15] and have been measured in Ref. [10]. However, there emerge several additional features. Most significantly in panel (i), we find that for the anti-symmetric driving with f_3, the structure is different from the corresponding $F(\tau_\epsilon/2)$ depicted by the dashed line in Fig. 1(c). Moreover, the driving f_2 yields further arcs close to the origin. There also emerge higher-order replica of the arcs which have been found both experimentally [14,15] and theoretically [14].

For an analytical approach to the arc structure, we consider $P_{\rm ex}(\epsilon_0, A) = \sum_n P_n^{(x)}(\epsilon_0, A)$ derived Sec. III B 2 and define its Fourier transform as

$$W(\tau_\epsilon, \tau_A) = \int \frac{d\epsilon_0}{2\pi} \frac{dA}{2\pi} e^{-i\epsilon_0\tau_\epsilon} e^{-iA\tau_A} P_{\rm ex}(\epsilon_0, A). \tag{23}$$

We neglect the background contribution $P_{\rm bg}$, because it varies on a scale much greater than Ω. Thus in Fourier space, it mainly contributes in the region $\tau_\epsilon, \tau_A \ll T$, i.e., very close to the origin. The ϵ_0 integral can be evaluated readily to yield

$$W(\tau_\epsilon, \tau_A) = \frac{1}{4\pi} \int dA\, e^{-iA\tau_A} \sum_n \frac{\Delta_n^2}{\Gamma_n^*} e^{-in\Omega\tau_\epsilon} e^{-\Gamma_n^*|\tau_\epsilon|}, \tag{24}$$

with the resonance width $\Gamma_n^* = (\Delta_n^2/2 + \Gamma^2/4)^{1/2}$.

A. Overdamped limit

The remaining A integral in Eq. (24) can be evaluated directly in the overdamped limit $\Gamma \gg \Delta$ in which $\Gamma_n^* \approx \Gamma/2$ and, thus,

$$W(\tau_\epsilon, \tau_A) = \frac{1}{2\pi\Gamma} \int dA e^{-iA\tau_A} \sum_n \Delta_n^2 e^{-in\Omega\tau_\epsilon}. \tag{25}$$

Focusing on the range of small τ_ϵ, we have neglected the last exponential of Eq. (24). To proceed, we evaluate the sum

$$\sum_n (\Delta_n)(\Delta_n e^{-in\Omega\tau_\epsilon}), \tag{26}$$

where the two factors are easily identified as the nth Fourier coefficients of $\exp\{-iAF(t)\}$ and $\exp\{-iAF(t+\tau_\epsilon)\}$, respectively; cf. the definition of Δ_n in Eq. (18). Thus, expression (26) represents the inner product of these exponentials. According to Parseval's theorem, it can be written in the time domain to read

$$\frac{1}{T} \int_0^T dt\, e^{iAF(t)} e^{-iAF(t+\tau_\epsilon)}. \tag{27}$$

We symmetrize the integrand via the substitution $t \to t - \tau_\epsilon/2$ and perform the A integration to obtain

$$W(\tau_\epsilon,\tau_A) = \frac{1}{T}\int_0^T dt\, \delta(\tau_A - G(t,\tau_\epsilon)) \tag{28}$$

$$= \frac{1}{T}\sum_{t_i}\frac{1}{|g(t_i,\tau_\epsilon)|}, \tag{29}$$

where

$$G(t,\tau_\epsilon) = F(t+\tau_\epsilon/2) - F(t-\tau_\epsilon/2), \tag{30}$$

$$g(t,\tau_\epsilon) = f(t+\tau_\epsilon/2) - f(t-\tau_\epsilon/2). \tag{31}$$

The sum in Eq. (29) has to be taken over all times t_i that fulfill $\tau_A = G(t_i,\tau_\epsilon)$.

Expressions (28) and (29) allow us to extract the arc structure by the following reasoning. On the one hand, the argument of the δ function in Eq. (28) specifies the times t_i that contribute to the integral. On the other hand, the most significant contributions to W stem from regions where the denominator in Eq. (29) vanishes. Thus, the structure is determined by the conditions

$$0 = g(t,\tau_\epsilon), \tag{32}$$

$$\tau_A = G(t,\tau_\epsilon), \tag{33}$$

which describe one-dimensional manifolds in the Fourier space (τ_ϵ,τ_A). They correspond to the arcs in Figs. 1(g)–1(i). In practice, the arc structure is obtained in the following way. One determines from $g(t_i,\tau_\epsilon) = 0$ all zeros $t_i(\tau_\epsilon)$ and inserts them into Eq. (33), which yields relations of the type $\tau_A^{(i)}(\tau_\epsilon)$.

Obviously, $\tau_A = \tau_\epsilon = t = 0$ is a trivial solution for any driving shape $f(t)$. Thus, the Fourier transform of any LZSM pattern exhibits a peak at the origin and, owing to the periodicity of the driving, at multiples of T.

Two generic arcs can be found analytically if the driving obeys time-reversal symmetry, $f(t-t_s) = f(-t-t_s)$ (without loss of generality, we henceforth assume $t_s = 0$). Then Eq. (32) possesses the solutions $t_1 = 0$ and, owing to the T periodicity of f, $t_2 = T/2$. They provide the arcs

$$\tau_A^{(1)} = 2F(\tau_\epsilon/2), \tag{34}$$

$$\tau_A^{(2)} = 2F(\tau_\epsilon/2 + T/2), \tag{35}$$

which are in agreement with Ref. [15].

If a symmetric driving f has only one minimum and one maximum per period, such as f_1 or $f(t) = \cos(\Omega t)$, t_1 and t_2 are the only roots of Eq. (32). Then the arc structure for symmetric driving can be obtained fully analytically. This knowledge facilitates the analysis if one employs LZSM interference to determine decoherence properties of a qubit via the arc decay [14].

In all other cases, i.e., when f is not symmetric or if it possesses more than two extrema per period, we have to solve Eq. (32) numerically to obtain also the "nongeneric" arcs. For the symmetric driving f_2, this leads to the ellipse-shaped solutions sketched in the lower panel of Fig. 5(a). Upon reducing the amplitude of the harmonic with frequency 2Ω, they shrink and eventually vanish. Together with the generic solution, we obtain the structure shown in the upper panel of Fig. 5(a). In particular, there is a region in which the arc splits into two branches. This prediction is quantitatively confirmed by the numerical solution of the full problem shown in Fig. 1(h).

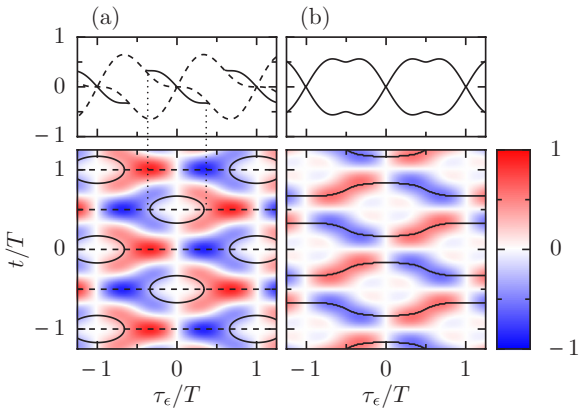

FIG. 5. (Color online) Determination of the "nongeneric" arcs for the driving shapes f_2 (a) and f_3 (b). The color code in the lower panels depicts $G(t,\tau_\epsilon)$, while the horizontal dashed lines mark the generic solutions of Eq. (32) at multiples of $T/2$. The solid lines represent numerical solutions of Eq. (32). Significant contributions to $W(\tau_\epsilon,\tau_A)$ are determined by the solutions of the transcendental equations (32) and (33), i.e., the cuts of $G(t,\tau_\epsilon)$ along the solid and dashed lines. Projection of these solutions on the τ_ϵ axis (hinted by vertical dotted lines) results in the arc structures plotted in the upper panels and in Figs. 1(h) and 1(i).

If f is not time-reversal symmetric, we generally have to determine all t_i numerically. For the driving shape f_3, this procedure is visualized in Fig. 5(b), where the solid lines in the lower panel depict the zeros of $g(t,\tau_\epsilon)$ which define two independent manifolds $t_i(\tau_\epsilon)$ and those related by the time shift $t \to t + T$. The corresponding arc structure shown in the upper panel agrees with the one obtained numerically that is shown in Fig. 1(i).

B. Weak dissipation

In the limit of weak dissipation, $\Gamma \ll \Delta_n$, the resonance width in Eq. (24) becomes $\Gamma_n^* = |\Delta_n|/\sqrt{2}$, so that we have to evaluate the Fourier transform of $\sum_n |\Delta_n(A)|$. This represents a rather difficult task and, thus, we discuss it only on a qualitative level.

A main effect of the cusps stemming from the absolute value is the emergence of higher harmonics; cf. the Fourier transform of expressions such as $|\cos(\Omega t)|$. Accordingly, in the Fourier transform of our interference patterns, we find arcs of higher order, as can be appreciated in Figs. 1(g)–1(i). To be specific, the arcs given by Eqs. (34) and (35) are generalized to

$$\tau_A = 2kF(\tau_\epsilon/2k + k'T/2k), \tag{36}$$

where $k = 1,2,3,\ldots$ and $k' = 0,1,\ldots,2k-1$. This prediction agrees with our numerical findings shown in Figs. 1(g) and 1(h). From a theoretical point of view, it is interesting to see that arcs of higher order are found already within a two-level description, i.e., within the most basic model for

LZSM interference. Thus, their emergence does not require the consideration of further levels or nonlinearities.

V. DECAY OF THE ARC STRUCTURE

A promising application of LZSM interferometry is to determine microscopic model parameters such as the dimensionless dissipation strength α. In Ref. [14], this was performed by comparing the decay of the arc structure of measured LZSM patterns with theoretical data. The underlying analysis requires that the decay is noticeably influenced by α and by the temperature. Therefore, we wish to explore numerically whether such a dependence can be found also for the present spin-boson model. Some examples for the arc decay are shown in Fig. 6(a). It can be appreciated that, in the vicinity of $\tau_\epsilon \approx T/4$, the Fourier amplitude decays exponentially, $W(\tau_\epsilon) \propto \exp(-\lambda\tau_\epsilon)$. This implies that there the decay can be characterized by one parameter only, namely, the rate λ which we determine within a numerical fit procedure. The central question is then whether λ exhibits a clear α dependence, in particular in the regime of low temperatures $\hbar\Omega\beta \gtrsim 1$ and small tunneling $\Delta \lesssim \hbar\Omega$, in which most LZSM patterns have been measured. Figures 6(b) and 6(c) show the decay rate as a function of the dissipation strength and the temperature, respectively.

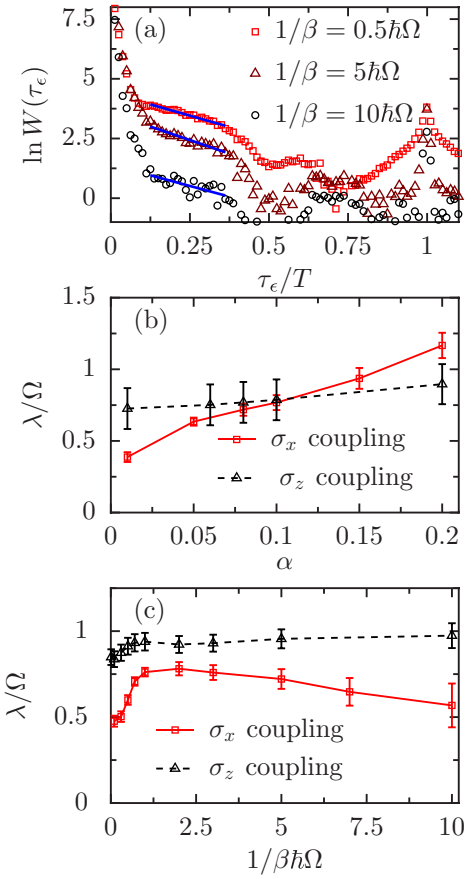

FIG. 6. (Color online) Analysis of the principal arc for the driving $f(t) = \cos(\Omega t)$ and system-bath coupling with $\Delta = 0.5\Omega$. (a) Fourier transform of the interference pattern, $W(\tau_\epsilon, \tau_A)$, along the principal arc $\tau_A = 2F(\tau_\epsilon/2)$ for σ_x coupling and $\alpha = 0.05$. The symbols show numerical results for different temperatures $1/\beta$, while the straight lines are fits to an exponential decay. (b) Decay rate λ for temperature $1/\beta = 0.5\hbar\Omega$ as a function of the dissipation strength α. The error bars are determined by slightly varying the fit range. (c) Decay rate as a function of the temperature for dissipation strengths $\alpha = 0.05$.

For longitudinal bath coupling, the rate exhibits a rather weak parameter dependence. A possible reason for this is that dissipative decays happen mainly during the short stages when the levels cross. Therefore the effective decoherence rate is always much smaller than the "natural" width of the asymmetric peaks given by Δ_n; cf. Fig. 4(a) and Eq. (22). At first sight, this weak parameter dependence seems not in accordance with the LZSM patterns for open quantum dots with a bath coupling via σ_z [14]. Notice however that the open double quantum dot used there is beyond the present model. First, the description of electron transport requires one to take more states and different electron numbers into account, especially when spin effects also play a role. Second, there the dot-lead coupling is responsible for the main dissipative effects, while the bath coupling represents a perturbation and does not influence the qualitative behavior.

For the transverse bath coupling via σ_x, by contrast, λ grows significantly and monotonically with the dissipation strength α, a feature that is essential for the fixing of α from measured data. The behavior as a function of the temperature is more involved and even nonmonotonic. For very low temperatures, the decay rate starts with a value $\lambda \approx 0.4\Omega$, followed by a steep increase until the thermal energy matches the photon energy. Then a slow decay sets in which lasts until eventually the range of exponential decay becomes so small that the fitting procedure is no longer reasonable.

VI. CONCLUSIONS

We have developed a comprehensive picture of LZSM interference for the spin-boson model and thereby extended previous results to arbitrary shapes of the periodic driving and a generalized qubit-bath coupling. Our central quantity of interest was the time-averaged population of the excited state of the undriven qubit. For its numerical computation, we have employed a Bloch-Redfield master equation decomposed into the Floquet states of the driven qubit, while avoiding any rotating-wave approximation even in its moderate form. Thus, our long-time solution contains the full information about the coherences.

The interference patterns in "real space", i.e., as a function of the detuning and the driving amplitude turned out to be governed by the qubit operator that couples to the environmental degrees of freedom. By contrast, the shape of the driving is of minor relevance. In particular, we found that for a bath coupling that is transverse with respect to the driving, the resonances are Lorentzians, while they possess an anti-symmetric structure in the longitudinal case. By a mapping to an effective static Hamiltonian we have obtained Bloch equations which yield expression for the LZSM patterns in agreement with numerical results. As a further feature, the LZSM pattern exhibits a triangular background which can be explained within an adiabatic approximation for the full time-dependent Bloch equations. Moreover, in the presence

of both a transverse and a longitudinal bath coupling, the influence of the transverse coupling prevails.

The Fourier transform of the LZSM patterns provides a complementary picture. This representation of the interference pattern is dominated by the shape of the driving manifest in the arc structure. The solution of our effective Bloch equations allowed us to generalize knowledge about these arcs. For a driving with time-reversal symmetry, they are given by the integral of the driving. In addition, they may develop side branches which can be explained within our analytical approach, but their determination requires the moderate effort of numerically solving a transcendental equation. The same numerical procedure also serves for the case of asymmetric driving.

A promising application of LZSM interferometry is the fixing of dissipative parameters by comparing the arc decay for experimental and theoretical data. In this spirit, we have performed the corresponding theoretical calculations. They show that for transverse bath coupling, the decay rate increases significantly with dissipation strength and temperature, as long as the thermal energy does not exceed the energy quantum of the driving. Thus, in particular for predominantly transverse coupling and low temperatures, LZSM interference represents a useful tools for analyzing decoherence properties. For purely longitudinal bath coupling, by contrast, the arc decay depends only weakly on dissipation.

Our investigation reveals that already the LZSM pattern of a qubit is quite intriguing. It may become even more involved for Landau-Zener scenarios with three or more levels [30,31] which are relevant when spin effects enter [32] or for a qubit that couples to additional degrees of freedom such as, e.g., an exciton in a photonic crystal with a coupling modulated by a surface acoustic wave [33]. LZSM interferometry for such setups represents an emerging field of investigation.

ACKNOWLEDGMENTS

We acknowledge helpful discussions with Florian Forster, Stefan Ludwig, Sergey Shevchenko, Daniel Domínguez, and Pavol Neilinger. This work was supported by the Deutsche Forschungsgemeinschaft via Sonderforschungsbereich SFB 631 (Project No. A5) and by the Spanish Ministerio de Economía y Competividad through Grant No. MAT2011-24331.

APPENDIX: BLOCH EQUATIONS

In order to derive an equation of motion for the *time-independent* qubit, we start from the master equation (4) and notice that for the Ohmic spectral density $J(\omega) = 2\pi\alpha\omega$, the antisymmetric bath correlation function (6) becomes $A(\tau) = 2\pi\alpha\delta'(\tau)$. This has for the τ integral in Eq. (4) the consequence that the Heisenberg operator $\tilde{X}$ turns into its time derivative evaluated at $\tau = 0$. Thus it can be expressed by the commutator $i[H,X]$, and we obtain

$$\dot{\rho} = -i[H,\rho] - \frac{1}{4}[X,[Q,\rho]] + \frac{\pi\alpha}{4}[X,\{[H,X],\rho\}], \quad \text{(A1)}$$

where the second term depends on the coherent qubit dynamics via the operator

$$Q = \frac{1}{2}\int_{-\infty}^{+\infty} d\tau\, S(\tau)\tilde{X}(-\tau). \quad \text{(A2)}$$

Since all analytical results of the main paper can be mapped by a permutation of the Pauli matrices to a qubit in its eigenbasis with a qubit-bath coupling via either $X = \sigma_x$ or $X = \sigma_z$, we consider the Hamiltonian

$$H = \frac{E}{2}\sigma_z. \quad \text{(A3)}$$

For $X = \sigma_x$, the Heisenberg operator in Eq. (A2) reads $\tilde{\sigma}_x(-\tau) = \sigma_x \cos(E\tau) - \sigma_y \sin(E\tau)$. With this expression at hand, it is straightforward to evaluate the operator Q and to map the master equation (A1) to an equation of motion for the Bloch vector $\vec{s} = \mathrm{tr}(\vec{\sigma}\rho)$. After some algebra and a rotating-wave approximation, we find the Bloch equation

$$\frac{d}{dt}\vec{s} = \begin{pmatrix} -\Gamma/2 & E & 0 \\ -E & -\Gamma/2 & 0 \\ 0 & 0 & -\Gamma \end{pmatrix}\vec{s} + \begin{pmatrix} 0 \\ 0 \\ \pi\alpha E \end{pmatrix}, \quad \text{(A4)}$$

where the rate

$$\Gamma = \pi\alpha E \coth(\beta E/2) \quad \text{(A5)}$$

depends on the qubit splitting and at low temperatures, $kT \ll E$, it becomes $\Gamma = \pi\alpha|E|$.

For σ_z coupling, the Heisenberg operator of the bath coupling is time independent, $\tilde{\sigma}_z(-\tau) = \sigma_z$, so that the τ integral yields the Fourier transform of the symmetric spectral density at zero frequency. Moreover, the last term of the master equation (A1) vanishes. Accordingly, the Bloch equation is homogeneous and reads

$$\frac{d}{dt}\vec{s} = \begin{pmatrix} -\Gamma\varphi & E & 0 \\ -E & -\Gamma\varphi & 0 \\ 0 & 0 & 0 \end{pmatrix}\vec{s}, \quad \text{(A6)}$$

where the dephasing rate

$$\Gamma_\varphi = 4\pi\alpha kT \quad \text{(A7)}$$

vanishes in the zero-temperature limit. Notice that the z component of the Bloch vector is conserved.

[1] L. D. Landau, Phys. Z. Sowjetunion **2**, 46 (1932).
[2] C. Zener, Proc. R. Soc. London, Ser. A **137**, 696 (1932).
[3] E. C. G. Stueckelberg, Helv. Phys. Acta **5**, 369 (1932).
[4] E. Majorana, Nuovo Cimento **9**, 43 (1932).
[5] S. N. Shevchenko, S. Ashhab, and F. Nori, Phys. Rep. **492**, 1 (2010).
[6] W. D. Oliver, Y. Yu, J. C. Lee, K. K. Berggren, L. S. Levitov, and T. P. Orlando, Science **310**, 1653 (2005).
[7] M. Sillanpää, T. Lehtinen, A. Paila, Y. Makhlin, and P. Hakonen, Phys. Rev. Lett. **96**, 187002 (2006).
[8] C. M. Wilson, T. Duty, F. Persson, M. Sandberg, G. Johansson, and P. Delsing, Phys. Rev. Lett. **98**, 257003 (2007).

[9] A. Izmalkov, S. H. W. van der Ploeg, S. N. Shevchenko, M. Grajcar, E. Il'ichev, U. Hübner, A. N. Omelyanchouk, and H.-G. Meyer, Phys. Rev. Lett. **101**, 017003 (2008).
[10] D. M. Berns, M. S. Rudner, S. O. Valenzuela, K. K. Berggren, W. D. Oliver, L. S. Levitov, and T. P. Orlando, Nature (London) **455**, 51 (2008).
[11] J. Stehlik, Y. Dovzhenko, J. R. Petta, J. R. Johansson, F. Nori, H. Lu, and A. C. Gossard, Phys. Rev. B **86**, 121303(R) (2012).
[12] E. Dupont-Ferrier, B. Roche, B. Voisin, X. Jehl, R. Wacquez, M. Vinet, M. Sanquer, and S. De Franceschi, Phys. Rev. Lett. **110**, 136802 (2013).
[13] J. Li, M. P. Silveri, K. S. Kumar, J.-M. Pirkkalainen, A. Vepsäläinen, W. C. Chien, J. Tuorila, M. A. Sillanpää, P. J. Hakonen, E. V. Thuneberg, and G. S. Paraoanu, Nat. Commun. **4**, 1420 (2013).
[14] F. Forster, G. Petersen, S. Manus, P. Hänggi, D. Schuh, W. Wegscheider, S. Kohler, and S. Ludwig, Phys. Rev. Lett. **112**, 116803 (2014).
[15] M. S. Rudner, A. V. Shytov, L. S. Levitov, D. M. Berns, W. D. Oliver, S. O. Valenzuela, and T. P. Orlando, Phys. Rev. Lett. **101**, 190502 (2008).
[16] M. Grifoni and P. Hänggi, Phys. Rep. **304**, 229 (1998).
[17] S. Kohler, T. Dittrich, and P. Hänggi, Phys. Rev. E **55**, 300 (1997).
[18] R. Blümel, A. Buchleitner, R. Graham, L. Sirko, U. Smilansky, and H. Walther, Phys. Rev. A **44**, 4521 (1991).
[19] J. Lehmann, S. Kohler, P. Hänggi, and A. Nitzan, Phys. Rev. Lett. **88**, 228305 (2002).
[20] F. Großmann and P. Hänggi, Europhys. Lett. **18**, 571 (1992).
[21] Y. Kayanuma, Phys. Rev. A **50**, 843 (1994).
[22] A. M. Satanin, M. V. Denisenko, A. I. Gelman, and F. Nori, Phys. Rev. B **90**, 104516 (2014).
[23] M. Strass, P. Hänggi, and S. Kohler, Phys. Rev. Lett. **95**, 130601 (2005).
[24] M. D. LaHaye, J. Suh, P. M. Echternach, K. C. Schwab, and M. L. Roukes, Nature (London) **459**, 960 (2009).
[25] P. Neilinger, M. Rehák, U. Hübner, E. Il'ichev, and M. Grajcar, Mach-Zehnder interferometry in an artificial quantum two level system, in *Proceedings of the 20th International Conference on Applied Physics of Condensed Matter* (FEI STU, Bratislava, 2014), pp. 26–29.
[26] J. Thingna, J.-S. Wang, and P. Hänggi, J. Chem. Phys. **136**, 194110 (2012).
[27] K. M. Fonseca-Romero, S. Kohler, and P. Hänggi, Chem. Phys. **296**, 307 (2004).
[28] T. M. Stace, A. C. Doherty, and S. D. Barrett, Phys. Rev. Lett. **95**, 106801 (2005).
[29] A. Ferrón, D. Domínguez, and M. J. Sánchez, Phys. Rev. Lett. **109**, 237005 (2012).
[30] M. N. Kiselev, K. Kikoin, and M. B. Kenmoe, Europhys. Lett. **104**, 57004 (2013).
[31] A. M. Satanin, M. V. Denisenko, S. Ashhab, and F. Nori, Phys. Rev. B **85**, 184524 (2012).
[32] H. Ribeiro, G. Burkard, J. R. Petta, H. Lu, and A. C. Gossard, Phys. Rev. Lett. **110**, 086804 (2013).
[33] R. Blattmann, H. J. Krenner, S. Kohler, and P. Hänggi, Phys. Rev. A **89**, 012327 (2014).